

Perovskite Solar Cells on Polymer-Coated Smooth and Rough Steel Substrates

Citation for published version (APA):

Feleki, B. T., Bouwer, R. K. M., Wienk, M. M., & Janssen, R. A. J. (2022). Perovskite Solar Cells on Polymer-Coated Smooth and Rough Steel Substrates. *Solar RRL*, 6(4), Article 2100898. <https://doi.org/10.1002/solr.202100898>

Document license:

CC BY-NC

DOI:

[10.1002/solr.202100898](https://doi.org/10.1002/solr.202100898)

Document status and date:

Published: 01/04/2022

Document Version:

Publisher's PDF, also known as Version of Record (includes final page, issue and volume numbers)

Please check the document version of this publication:

- A submitted manuscript is the version of the article upon submission and before peer-review. There can be important differences between the submitted version and the official published version of record. People interested in the research are advised to contact the author for the final version of the publication, or visit the DOI to the publisher's website.
- The final author version and the galley proof are versions of the publication after peer review.
- The final published version features the final layout of the paper including the volume, issue and page numbers.

[Link to publication](#)

General rights

Copyright and moral rights for the publications made accessible in the public portal are retained by the authors and/or other copyright owners and it is a condition of accessing publications that users recognise and abide by the legal requirements associated with these rights.

- Users may download and print one copy of any publication from the public portal for the purpose of private study or research.
- You may not further distribute the material or use it for any profit-making activity or commercial gain
- You may freely distribute the URL identifying the publication in the public portal.

If the publication is distributed under the terms of Article 25fa of the Dutch Copyright Act, indicated by the "Taverne" license above, please follow below link for the End User Agreement:

www.tue.nl/taverne

Take down policy

If you believe that this document breaches copyright please contact us at:

openaccess@tue.nl

providing details and we will investigate your claim.

Perovskite Solar Cells on Polymer-Coated Smooth and Rough Steel Substrates

Benjamin T. Feleki, Ricardo K. M. Bouwer, Martijn M. Wienk, and René A. J. Janssen*

Fabricating efficient perovskite solar cells on steel substrates could enable easy building integration of this photovoltaic technology. Herein, an n–i–p perovskite solar cell is developed on steel substrates for top illumination. The optimized stack uses a Ti bottom electrode, covered with an indium tin oxide (ITO) interlayer and a SnO₂ electron transport layer passivated by [6,6]-phenyl-C₆₁-butyric acid. The active layer is a triple-cation perovskite. A thermally evaporated tris(4-carbazoyl-9-ylphenyl)amine)/MoO₃ bilayer acts as hole transport layer. The transparent top contact consists of ITO with a MgF₂ antireflective coating. Optical analysis shows small parasitic absorption and reflectance losses for this stack, which provides 15.9% power conversion efficiency when fabricated on glass. On steel, covered with a polyamide imide planarization coating to moderate the surface roughness (R_p), the highest efficiency is 15.2% for high-gloss steel ($R_p \approx 200$ nm), 14.9% for battery steel ($R_p \approx 500$ nm), 14.2% for packaging steel ($R_p \approx 1500$ nm), and 13.8% for construction steel ($R_p \approx 2500$ nm). While the short-circuit current density and open-circuit voltage are invariant, the fill factor decreases with increasing R_p due to increasing series resistance and decreasing shunt resistance. The yield of working devices remain high, also for the roughest substrates.

1. Introduction


Building integration of perovskite solar cells could 1 day become feasible because of their low cost, aesthetics, lightweight, and impressive power conversion efficiency (PCE).^[1–5] When focusing on potential substrate materials compatible with the building industry, coated steel offers an interesting perspective because it is one of the most common architectural materials, especially in industrial buildings. Steel is a cheap (substrate) material and offers excellent mechanical, heat resistance, and barrier properties against oxygen and humidity.^[6,7] Combining perovskite solar cells with steel can give added value to this commonly employed building material. One of the challenges to tackle when fabricating solar cells directly on steel substrates is the higher surface roughness as compared to glass or polymer film which can be fatal for thin-film solar cells. Using smooth steel substrates would add to the cost due to the extra surface polishing steps. The cost can be reduced when combining rough steel substrates with an additional planarization layer.^[8]

Fabricating perovskite solar cells on rough substrates may reduce device performance and yield, due to irregularities such as spike-like protrusions, valleys, and peaks. To investigate the impact of surface roughness on the photovoltaic performance, we developed a substrate-configuration n–i–p solar cell for coated steel substrates (**Figure 1**). Fabrication of perovskite solar cells on rough substrates has been mostly studied in superstrate-configuration single-junction and top-illuminated perovskite Si monolithic tandem solar cells.^[9–15] In several studies on tandem solar cell applications a rough pyramidal-textured Si substrate has been used. To achieve a conformal coverage of the perovskite active layer, the perovskite layer needs to be sufficiently thick, or it needs to be deposited via co-evaporation^[9–11] or a hybrid evaporation/spin coating deposition method.^[12–14] Tockhorn et al. demonstrated conformal coating of the perovskite active layer in single-junction superstrate-configuration perovskite solar cells by employing a self-assembled [2-(9H-carbazol-9-yl)ethyl]phosphonic acid (2PACz) monolayer hole transport layer (HTL) on a nanotextured indium tin oxide (ITO) glass substrate providing 19.7% efficiency.^[15] In substrate-configuration perovskite solar cells, most devices have been fabricated on polished Ti foils, reaching efficiencies up to 15%.^[16] Although most studies on substrate-configuration perovskite solar cells use polished Ti

B. T. Feleki, M. M. Wienk, R. A. J. Janssen
Molecular Materials and Nanosystems and Institute for Complex
Molecular Systems
Eindhoven University of Technology
5600 MB Eindhoven, The Netherlands
E-mail: r.a.j.janssen@tue.nl

R. K. M. Bouwer
Surface Engineering – Coating Development
Tata Steel, Research and Development
1951 JZ Velsen-Noord, The Netherlands

R. A. J. Janssen
Dutch Institute for Fundamental Energy Research
5612 AJ Eindhoven, The Netherlands

 The ORCID identification number(s) for the author(s) of this article can be found under <https://doi.org/10.1002/solr.202100898>.

© 2021 The Authors. Solar RRL published by Wiley-VCH GmbH. This is an open access article under the terms of the Creative Commons Attribution-NonCommercial License, which permits use, distribution and reproduction in any medium, provided the original work is properly cited and is not used for commercial purposes.

DOI: 10.1002/solr.202100898

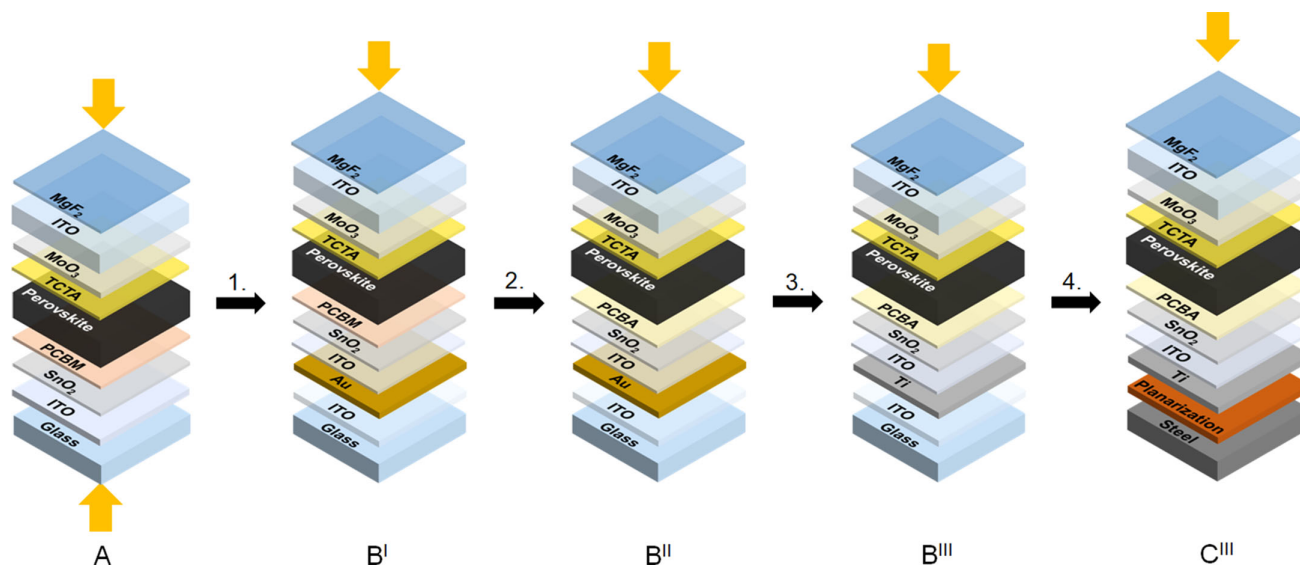


Figure 1. Stepwise transformation of a semitransparent perovskite solar cell (A), via cells with an opaque metal bottom electrode on glass (B', B'', and B'''), to a substrate-configuration cell on steel (C'''). Metal is Au in B' and B'', and Ti in B''' and C'''. Passivation is PCBM in A and B', and PCBA in B'', B''', and C'''. Details of the layer thicknesses are collected in Table S1, Supporting Information. The arrows indicate the direction of incoming sunlight.

foils, the impact of substrate surface roughness as an important parameter for future upscaling was not investigated.

Herein, we have developed a substrate-configuration n-i-p perovskite solar cell for integration with polymer-coated steel substrates and investigate the influence of the substrate surface roughness on the photovoltaic parameters. We start from a semitransparent n-i-p perovskite solar cell on an ITO-covered glass substrate having a transparent ITO top electrode coated with an antireflective coating. In a stepwise fashion we transformed this cell into an optimized substrate-configuration device stack with an opaque Ti bottom electrode. Fabricated on glass, this opaque cell gave 15.9% PCE with top illumination, and the PCE dropped only slightly when fabricated on different surface quality polymer-coated steel substrates to reach PCEs between 15.2% for high gloss steel and 13.8% for construction steel. The increase in surface roughness of the substrate was found to mainly affect the fill factor (FF) of the cells but not the short-circuit current density (J_{sc}), open-circuit voltage (V_{oc}), or fabrication yield of working devices.

2. Results and Discussion

The modification steps in transforming a semitransparent solar cell fabricated on glass, via a top-illuminated device with an opaque metal bottom electrode, into a cell that can be fabricated on steel are shown in Figure 1. The different layer thicknesses in these stacks are collected in Table S1, Supporting Information and the cells are discussed in detail in the next subsections.

2.1. Semitransparent Cells

A key aspect of an efficient substrate-configuration perovskite solar cell is the use of a transparent top electrode that enables in-

coupling of the light that is to be absorbed by the perovskite semiconductor. In a n-i-p configuration, this not only requires the use of a transparent n electrode, but also a weakly absorbing, transparent HTL. We have recently shown that thin (7–10 nm), pristine, thermally evaporated organic HTLs can significantly reduce the parasitic absorption by the HTL compared to the more commonly used thick and doped Spiro-OMeTAD layers.^[17] Here, we used tris(4-carbazoyl-9-ylphenyl)amine (TCTA). To protect the thin TCTA layer against damaging, it was covered with a layer of thermally-evaporated MoO₃ before depositing ITO by sputtering. To reduce reflection of light caused by the high-refractive index ITO top contact, we employed a thermally evaporated MgF₂ antireflective coating. To test the performance of the TCTA/MoO₃/ITO/MgF₂ top contact, we fabricated a semitransparent perovskite solar cell (Figure 1, stack A). In this cell, the bottom contact consists of an ITO-covered glass substrate with a SnO₂ electron transport layer (ETL) deposited from an aqueous SnO₂ nanoparticle dispersion and passivated with [6,6]-phenyl-C₆₁-butyric acid methyl ester (PCBM). As active layer, we used a triple-cation Cs_{0.05}(MA_{0.17}FA_{0.83})_{0.95}Pb(I_{0.83}Br_{0.17})₃ perovskite (MA is methylammonium, FA is formamidinium).^[18] The current density–voltage (J – V) characteristics for this cell recorded under simulated AM1.5G (air mass 1.5 global) solar light provided a stabilized PCE of 16.1% when illuminated from the bottom side (glass/ITO). This cell provided a $J_{sc,EQE}$ of 19.7 mA cm⁻², obtained via integration of the external quantum efficiency (EQE) spectrum with the standard AM1.5G solar spectrum, a V_{oc} of 1.17 V, and a FF of 0.70 (Figure 2a and Table 1). With top-side (ITO/MgF₂) illumination the same device reached a nearly identical PCE of 16.7% with very similar $J_{sc,EQE}$ (19.5 mA cm⁻²), V_{oc} (1.17 V), and FF (0.73) (Table 1). Differences in the shape and magnitude of the EQE spectra between the two illumination directions are minimal (Figure 2b). The reduced EQE for wavelengths below 400 nm with top-side illumination are caused by the parasitic absorption of light

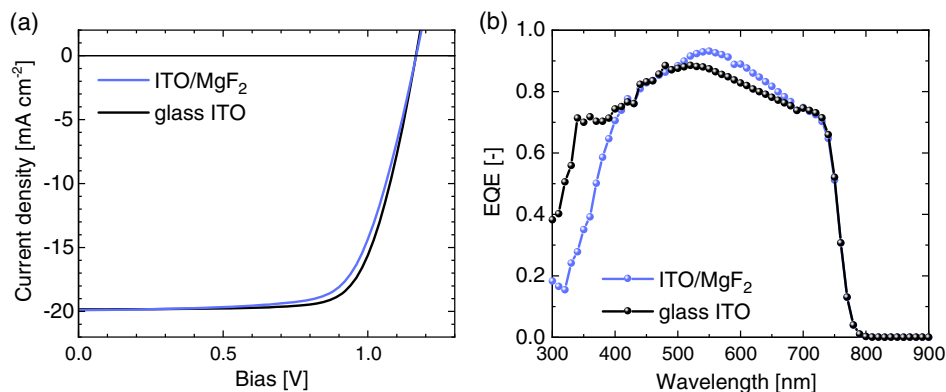


Figure 2. a) Stabilized J - V characteristics of semitransparent solar cells (stack A) with a triple-cation $\text{Cs}_{0.05}(\text{MA}_{0.17}\text{FA}_{0.83})_{0.95}\text{Pb}(\text{I}_{0.83}\text{Br}_{0.17})_3$ perovskite active layer, illuminated from bottom side (glass/ITO) and top side (ITO/ MgF_2) with simulated AM1.5G light (100 mW cm^{-2}). b) Corresponding EQE spectra.

Table 1. Stabilized J - V parameters of the optimized semitransparent perovskite solar cell with bottom (glass/ITO) and top (ITO/ MgF_2) illumination with simulated AM1.5 G light.

Illumination	J_{sc} [mA cm^{-2}]	$J_{sc,EQE}$ [mA cm^{-2}]	V_{oc} [V]	FF [-]	PCE [%]	PCE_{EQE} [%]
Glass/ITO	19.9	19.7	1.17	0.70	16.3	16.1
ITO/ MgF_2	19.8	19.5	1.17	0.73	16.9	16.7

by the sputtered amorphous ITO top electrode. Concomitantly, the higher EQE values with top-side illumination for wavelengths above 500 nm are due to a reduced reflection owing to the antireflective MgF_2 coating. From these results, we conclude that the use of a thin TCTA/ MoO_3 HTL in combination with an ITO/ MgF_2 electrode results in minimal optical losses with top illumination compared to bottom illumination from via the glass/ITO/ SnO_2 /PCBM layers.

2.2. Opaque Substrate-Configuration Cells on Glass

In the next steps (A \rightarrow B^I, B^{II}, and B^{III}), we fabricated opaque substrate-configuration solar cells on glass substrates. The prime reason to use glass in this step of the optimization is to first exclude effects of surface roughness introduced by the steel substrates. We started with a highly reflective opaque Au bottom electrode, which was covered with a thin (10 nm) sputtered ITO interlayer to significantly improve the wetting of the aqueous SnO_2 nanoparticle dispersion used for depositing the ETL on the hydrophobic Au bottom electrode via spin coating. The SnO_2 ETL was passivated with PCBM (B^I stack) or with [6,6]-phenyl- C_{61} -butyric acid (PCBA) (B^{II} stack). By binding to the SnO_2 , PCBA is better retained during processing of the $\text{Cs}_{0.05}(\text{MA}_{0.17}\text{FA}_{0.83})_{0.95}\text{Pb}(\text{I}_{0.83}\text{Br}_{0.17})_3$ absorber layer on top.^[19] While passivation of SnO_2 with PCBA does not increase the maximum PCE compared to PCBM, it dramatically increases the yield of efficient devices and reduces the spread as shown in **Figure 3a,c**. Under slow sweep conditions the best PCBA-passivated (B^{II} stack) cell reached 16.1% efficiency, compared to 17.4% for the best cell with PCBM-passivation (B^I stack)

(**Table 2**). The much higher yield of well-performing B^{II}-stack devices is a consequence of a significantly better wetting of the perovskite precursor solution on the PCBA-passivated SnO_2 than on PCBM-passivated SnO_2 (Figure S1, Supporting Information), which leads to a significant reduction of shorted devices and much less spread in the device performance (Figure 3c). The lower $J_{sc,EQE}$ for the best B^{II} device compared to the best B^I cell is due to a slight reduction in the EQE values over the relevant wavelength regime (Figure 3b) and can be explained by variations in layer thicknesses. The second modification (B^{II} \rightarrow B^{III}) involved replacing the Au bottom electrode with a Ti bottom electrode. Compared to Au, Ti is more cost effective and is commonly used as bottom electrode in substrate-configuration n-i-p perovskite solar cells. Ti did not alter the J - V characteristics significantly and the cell reproducibility remained good (Figure 3a,c). The best performing B^{III} substrate cell reached a PCE of 15.9% with lower $J_{sc,EQE}$ (19.5 mA cm^{-2}) but slightly higher V_{oc} (1.15 V) and FF (0.70) compared to best Au-based (B^{II}) cell (Table 2). The reduced $J_{sc,EQE}$ for the Ti-based devices is due to the slightly lower EQE above 550 nm (Figure 3b), owing to reduced reflection from the Ti bottom electrode compared to Au.

The simulated optical absorption and reflection caused by the individual layers in stack B^{II} and B^{III} cells with Au and Ti bottom electrodes are visualized in **Figure 4**. The figure shows the product of the absorptance of the various layers (or cell reflectance) with the AM1.5G photon flux Φ [#photons $\text{m}^{-2} \text{s}^{-1} \text{nm}^{-1}$] as function of wavelength. **Table 3** summarizes the corresponding contributions to and losses of photocurrent as the product of the elementary charge q [C] and Φ that is reflected, transmitted, or absorbed after integration over the relevant spectral range of the two cells.

The simulated total optical loss in the Ti-based B^{III} stack is 2.8 mA cm^{-2} , compared to 2.2 mA cm^{-2} for the Au-based B^{II} stack (Table 3). In both solar cells, the main optical losses are caused by reflection of light from the top MgF_2 coating (0.8 – 0.9 mA cm^{-2} , red areas in Figure 4), absorption of light by the ITO top electrode (1.0 mA cm^{-2} , yellow areas in Figure 4), and the MoO_3 buffer layer (0.2 mA cm^{-2} , blue areas in Figure 4). The main difference between the two stacks is the increased absorption of light by the Ti bottom electrode

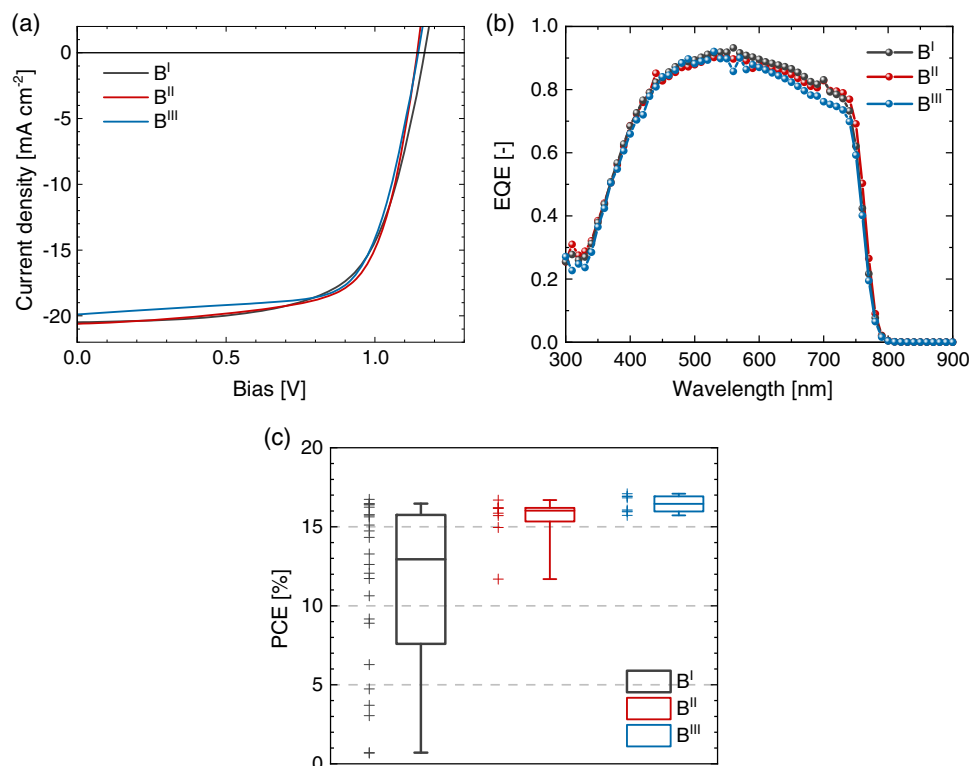


Figure 3. a) Stabilized J - V characteristics of perovskite solar cells with an Au/ITO (B^I, B^{II}) or Ti/ITO (B^{III}) bottom electrode and a SnO₂ ETL passivated with PCBM (B^I) or PCBA (B^{II}, B^{III}) illuminated with simulated AM1.5G light (100 mW cm⁻²). b) Corresponding EQE spectra. c) PCE statistics for the three configurations, measured in fast downward sweeps.

Table 2. Stabilized J - V parameters of optimized substrate-configuration perovskite solar cells (B^I, B^{II}, and B^{III} stacks).

Stack	J_{sc} [mA cm ⁻²]	$J_{sc,EQE}$ [mA cm ⁻²]	V_{oc} [V]	FF [-]	PCE [%]	PCE _{EQE} [%]	Yield ^{a)}
B ^I	21.2	21.1	1.16	0.71	17.4	17.4	8/16
B ^{II}	20.6	20.5	1.14	0.69	16.1	16.1	7/8
B ^{III}	19.9	19.9	1.15	0.70	15.9	15.9	8/8

^{a)}The number of properly working cells/the total number of cells.

(0.8 mA cm⁻²) compared to (0.1 mA cm⁻²) for the Au bottom electrode (cyan areas in Figure 4). As a consequence, the estimated maximum photocurrent generated by the perovskite layer is 22.0 mA cm⁻² for the Ti-based B^{III} stack compared to 23.0 mA cm⁻² for the Au-based B^{II} stack. Comparison with the experimental values of 19.9 mA cm⁻² for B^{III} and 20.5 mA cm⁻² for B^{II}, provides estimates for the AM1.5G-averaged internal quantum efficiency (IQE) of 90% and 89%, respectively. The analysis shows that the absorption of photons by this Ti limits the photocurrent to some extent. Other cost-effective, but more reflective metals such as Cu are frequently used together with an ITO diffusion barrier in crystalline-Si solar cells and could possibly enhance the maximum attainable photocurrents to the level of a B^{II} stack with a Au bottom electrode.^[20–22]

2.3. Cells on Polymer-Coated Smooth and Rough Steel Substrates

In a final step (B^{III}→C^{III}), perovskite solar cells were fabricated on polymer-coated steel substrates. To assess the impact of surface roughness on the photovoltaic parameters, steel samples with widely different surface roughness were used. We selected a Ni-plated high-gloss steel (R1), Ni-plated battery steel (R2), Cr-plated packaging steel (R3), and Zn-coated construction steel (R4). For future integration of perovskite solar cells in steel buildings, the devices will eventually be deposited directly on the polymer-coated steel itself. A typical coating for such steels consists of a primer layer followed by a topcoat layer both with a thickness range in the order of 10–200 μm. These coatings typically consist of commodity polymers like polyester for the lower end of the product portfolio to polyvinylidene fluoride (PVDF) and polyurethane (PU) for more demanding, higher end, applications. These coated products often come with lifetime guarantees of 15 up to 40 years of corrosion protection and offer excellent resistance to ambient conditions in various environments. However, to avoid any incompatibilities with the processing of the perovskite solar cells, a more inert polyimide-amide (Torlon) coating was chosen as planarization layer to reduce roughness and insulate the substrate from the bottom electrode. Electrical insulation is necessary if multiple cells are interconnected on a substrate and for building integration.

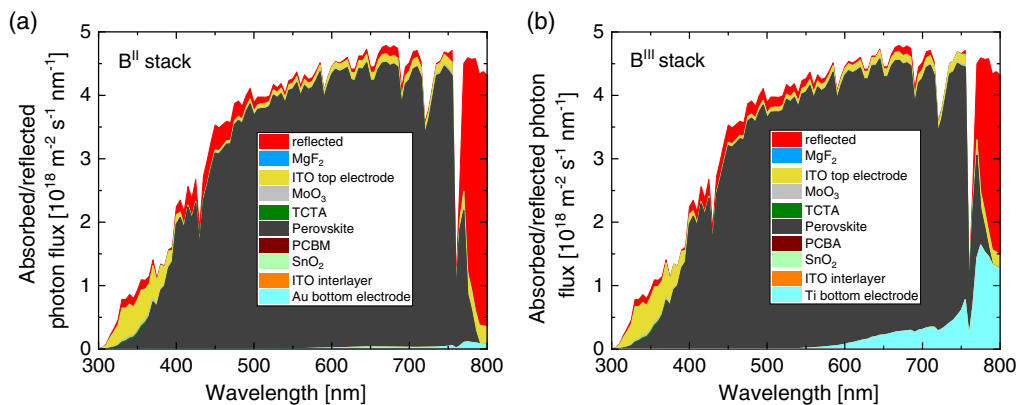


Figure 4. The AM1.5G photon flux reflected, transmitted, or absorbed by each individual layer in the a) B^{II} and b) B^{III} substrate-configuration cells with Au and Ti bottom electrodes, respectively.

Table 3. Integrated AM1.5 G photocurrent absorbed or reflected by each layer in opaque substrate-configuration cells with Au (B^{II}) and Ti (B^{III}) bottom electrodes.

Layer	Thickness [nm]	Au (B ^{II})	Ti (B ^{III})
		$q\Phi$ [mA cm ⁻²]	$q\Phi$ [mA cm ⁻²]
Air (reflected)	∞	0.9	0.8
MgF ₂	90	≈0	≈0
ITO top electrode	180	1.0	1.0
MoO ₃	15	0.2	0.2
TCTA	10	≈0	≈0
Cs _{0.05} (MA _{0.17} FA _{0.83}) _{0.95} Pb(I _{0.83} Br _{0.17}) ₃ ^{a)}	600	23.0	22.0
PCBA	1	≈0	≈0
SnO ₂	85	≈0	≈0
ITO	10	≈0	≈0
Au/Ti bottom electrode	120	0.1	0.8
Air (transmitted)	∞	≈0	≈0

^{a)}Integration from 300 to 755 nm, for all layers except for the perovskite layer where integration was up to 800 nm.

The surface roughness, represented by the maximum profile peak height above the mean line (R_p), determined with surface profilometry of the glass/ITO and PAI-coated steel substrates varied between roughly between 200 and 3000 nm (Table 4 and Figure 5). The substrates exhibit very different macroscopic surface textures depending on their surface finishing. While the glass/ITO and R1 substrates show fairly smooth surface textures with only small protrusions, R2 and R3 substrates yield a macroscopic surface texture with a linear orientation. The R4 substrate is very different, and its texture can be described with randomly appearing macroscopic hills and valleys. To evaluate the microscopic surface roughness, AFM measurements were performed (Figure 6). The microscopic root-mean-squared surface roughness (R_q) of the glass/ITO substrate is 2.2 nm with a R_p of 10 nm (Table 4). All PAI-coated steel substrates gave consistently lower microscopic R_q values between 1.0 and 1.4 nm

(Table 4). The corresponding R_p values were between 7 and 40 nm and are due to the presence of small protrusions visible as white spots in the AFM images. Differences in R_p values between the two profilometric measurements are related to the significantly smaller scanning area ($5 \times 5 \mu\text{m}^2$) in AFM compared to the surface profiler ($2 \times 2 \text{mm}^2$).

Interestingly, the photovoltaic performance and efficiency of Ti-based coated steel substrate cells (C^{III}) decreased only slightly with increasing surface roughness (Figure 7a, Table 5) and the reproducibility in the performance and the yield of properly working cells remained virtually unaffected (Figure 8, Table 5). Cells on steel substrates show stable operation under maximum power point tracking for 5 min. as shown in Figure S2, Supporting Information. The best C^{III} cell on steel gave a PCE of 15.2%, which is only slightly less than the 15.9% for the best B^{III} device on glass/ITO (Table 5). The stabilized efficiencies of the best C^{III} cells dropped from 15.2% for R1 to 13.8% for R4 substrate with increasing roughness as measured with the profilometer. The efficiency drop is mainly caused by a decrease in FF which decreased from 0.70 (glass/ITO) and 0.67 (R1) to 0.60 (R4). The $J-V$ characteristics (Figure 7a) show that the reduction in FF is due to a combination of an increased series resistance and decreased shunt resistance which both evolve progressively going from R1 to R4. The reduced shunt resistance is expected when the perovskite layer thickness drops locally, while the increased series resistance may originate from local poor or absent electrical contacts between adjacent layers. For R4 substrates, some cells gave S-shaped $J-V$ characteristics, which could be related to such a poor contact with an energetic

Table 4. R_q and R_p roughness of the glass/ITO and PAI-coated steel substrates R1 to R4.

Substrate type	R_q [nm]	R_p [nm]	R_p [nm]
	AFM	AFM	Profilometer
Glass/ITO	2.2	10	260
Ni-plated high gloss steel (R1)	1.0	40	220
Ni-plated battery steel (R2)	1.4	10	510
Cr-plated packaging steel (R3)	1.0	10	1500
Zn-coated construction steel (R4)	1.3	20	2600

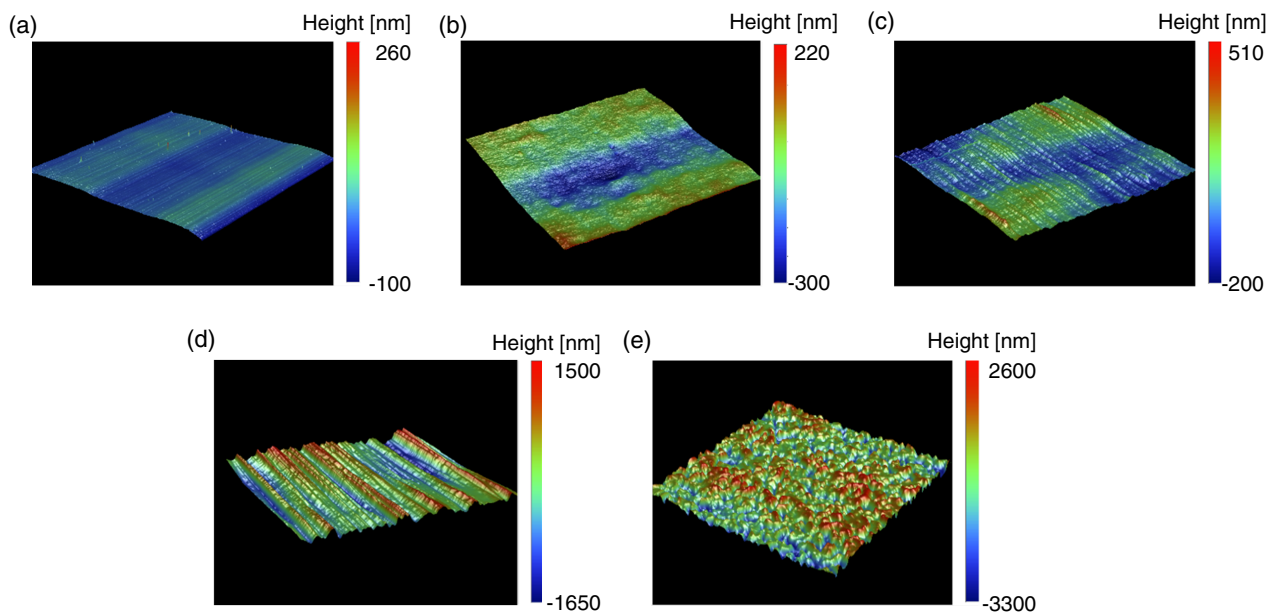


Figure 5. 3D surface height maps ($2 \times 2 \text{ mm}^2$) of a) glass/ITO and b–e) PAI-coated steel substrates R1–R4. The color bars represent different height scales. a) 360 nm. b) 420 nm. c) 810 nm. d) 3150 nm. e) 5900 nm.

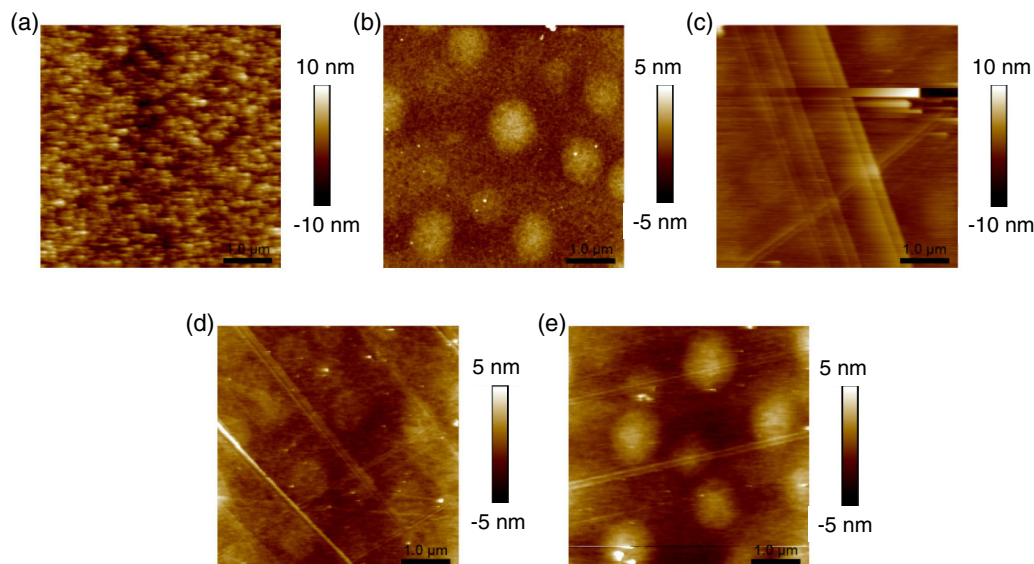


Figure 6. AFM height images ($5 \times 5 \mu\text{m}^2$) measured on a) glass/ITO and b–e) PAI-coated steel substrates R1–R4.

barrier. While the R_p roughness affected the FF it had a negligible impact on the $J_{sc,EQE} \approx 20 \text{ mA cm}^{-2}$ and on the shape of the EQE spectra (Figure 7b). Similarly, the V_{oc} was almost identical ($\approx 1.15 \text{ V}$) for all the substrate variations.

Charge recombination in B^{III} and C^{III} cells on glass/ITO and PAI-coated steel substrates was investigated by measuring the V_{oc} as function of photon flux (Figure 7c). The ideality factor determined from the slope of the semilogarithmic plot was estimated to be $n = 1.64\text{--}1.73$ on coated steel substrates with a C^{III} stack, compared to $n = 1.75$ for the best B^{III} cell on the glass/ITO substrate. With increasing surface roughness the ideality factor

increased but at 1 sun light intensity the V_{oc} values are virtually identical. The increase of n with increasing R_p could originate from small shunts that are more pronounced in cells fabricated on rougher substrates.^[23]

It is worth mentioning that the best device on a PAI-coated steel substrate gave a slightly higher PCE than the best Ti-based single-junction cell reported so far in the literature with 15%.^[16] Although the best device with a Ti-bottom electrode gave significantly higher V_{oc} and $J_{sc,EQE}$ values, the FF leaves room for further improvement. This can possibly be achieved by reducing resistive losses in the n–i–p substrate cell by improving interlayer or top contacts.

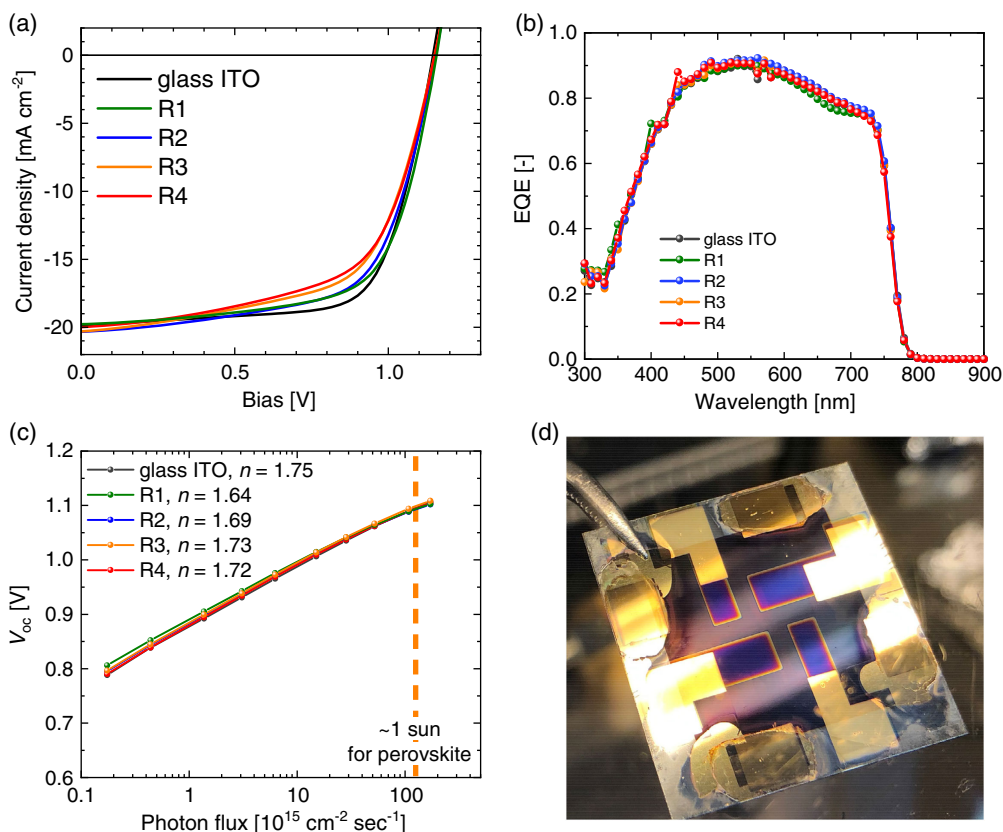


Figure 7. a) Stabilized J - V characteristics of substrate perovskite solar cells with an ITO interlayer coated opaque Ti bottom electrode on glass/ITO substrate (B^{III} stack) and coated steel substrates (C^{III} stack on R1–R4), illuminated with simulated AM1.5G light (100 mW cm⁻²). b) Corresponding EQE spectra. c) Corresponding light intensity dependence of V_{oc} . d) Photograph of the four best C^{III} devices on a R1 coated steel substrate.

Table 5. Stabilized J - V parameters of the optimized substrate-configuration perovskite solar cells with a Ti bottom electrode on glass/ITO (B^{III}) and PAI-coated steel (C^{III}, R1–R4).

Substrate	J_{sc} [mA cm ⁻²]	$J_{sc,EQE}$ [mA cm ⁻²]	V_{oc} [V]	FF [-]	PCE [%]	PCE _{EQE} [%]	Yield ^{d)}
Glass/ITO	19.9	19.9	1.15	0.70	15.9	15.9	8/8
R1	19.8	19.8	1.16	0.67	15.2	15.2	11/12
R2	20.3	20.2	1.15	0.64	15.0	14.9	6/8
R3	20.3	20.1	1.15	0.61	14.2	14.1	7/8
R4	20.0	20.0	1.15	0.60	13.8	13.8	7/8

^{d)}The number of properly working cells/the total number of cells.

3. Conclusions

In summary, we have developed an optimized n-i-p device stack for substrate-configuration perovskite solar cells on polymer-coated steel substrates and investigated the impact of surface roughness on the J - V characteristics. The optimized stack has an opaque Ti/ITO/SnO₂/PCBA bottom contact for electron collection and a TCTA/MoO₃/ITO/MgF₂ transparent top contact for

hole collection. When deposited on a glass substrate, the cell reached 15.9% PCE, which was only slightly limited by absorption of light by the Ti bottom electrode, while other photon losses were mainly due to reflection and parasitic absorption by the top ITO contact. The impact of the substrate surface roughness on the photovoltaic performance was investigated by fabricating the same device stack on four different planarization layer coated steel substrates with increasing macroscopic surface roughness. The cells reached stabilized PCEs of 15.2% on a high gloss steel ($R_p \approx 200$ nm), 14.9% on battery steel ($R_p \approx 500$ nm), 14.1% on packaging steel ($R_p \approx 1500$ nm), and 13.8% on a construction steel ($R_p \approx 2500$ nm). With increasing surface roughness the FF showed a gradual decrease as a result of increasing series resistance and a reduced shunt resistance, while the J_{sc} and V_{oc} remained nearly unchanged. Also the yield of working devices and the statistics of the photovoltaic parameters was not really affected by the surface roughness. This demonstrates that developed device stack is fairly robust against the roughness of the substrate.

The reduced FF with increasing surface roughness seems to originate from an increased series resistance and a lower shunt resistance. The latter is not unexpected and can be understood by considering thickness variations and nonconformal or local absence of layer coverage by small protrusions. The increased series resistance could find its origin in localized regions where

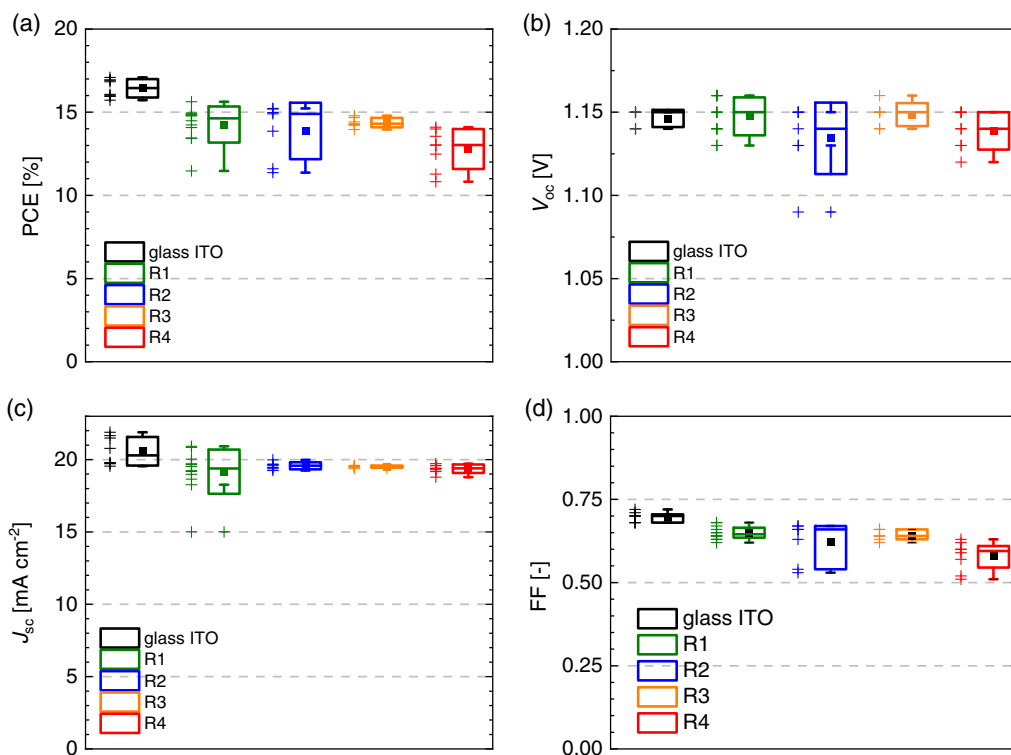


Figure 8. Fast-scan photovoltaic (PV) characteristics of substrate perovskite solar cells with Ti bottom electrodes on glass/ITO (B^{III} stack) and PAI-coated steel substrates (C^{III} stack on R1–R4), illuminated with simulated AM1.5G light (100 mW cm^{-2}).

electrical contact between adjacent layers is absent or insufficient. In such case the series resistance would increase, the photocurrent would become electric-field dependent as seen in Figure 7a, S-shaped J - V characteristics (as seen for the roughest substrates) may develop. Hence, while the PCEs are remarkably high for very rough steel substrates, an improved control over conformity may lead to further improvements.

4. Experimental Section

Materials and Preparation of Solutions: All materials and reagents were purchased from commercial sources. Solutions were stirred at 60°C overnight before the spin coating, unless stated otherwise. The starting point was a semitransparent n-i-p cell (A stack) with an ITO bottom electrode and a MgF_2 -coated ITO transparent top electrode. For the ETL, a commercial 15 wt% SnO_2 aqueous colloidal dispersion (Alfa Aesar) was used without dilution. The dispersion was stirred overnight at room temperature. For semitransparent A and substrate-configuration B^I cells, [6,6]-phenyl-C₆₁-butyric acid methyl ester (PCBM) (Solenne BV, 99%) was dissolved in chlorobenzene (Sigma-Aldrich, anhydrous 99.8%) at a concentration of 10 mg mL^{-1} . For substrate-configuration B^{II}, B^{III}, and C^{III} cells, [6,6]-phenyl-C₆₁-butyric acid (PCBA) was dissolved in 1,2-dichlorobenzene (Sigma-Aldrich, anhydrous 99%) at 0.2 mg mL^{-1} . For the triple-cation $\text{Cs}_{0.05}(\text{MA}_{0.17}\text{FA}_{0.83})_{0.95}\text{Pb}(\text{I}_{0.83}\text{Br}_{0.17})_3$ perovskite precursor solution,^[18] PbI_2 (576 mg) (TCI Chemicals, 99.99% trace metal basis) and PbBr_2 (550.5 mg) (TCI Chemicals, 99.99% trace metal basis) were dissolved separately in a mixture of *N,N*-dimethylformamide (DMF) (0.8 mL) and dimethyl sulfoxide (DMSO) (0.2 mL). Then 0.936 mL of the PbI_2 solution was added to formamidinium iodide (FAI) (200 mg) (Greatcell Solar), and 0.702 mL of the PbBr_2 solution was added to methylammonium bromide (MABr) (99.7 mg) (Greatcell Solar). Finally, 0.833 mL of the PbI_2 -FAI solution,

0.167 mL of the PbBr_2 -MABr, and 50 μL CsI (Sigma Aldrich, 99.999%) of a stock solution of 389.7 mg mL^{-1} in DMSO (Sigma-Aldrich, anhydrous 99.9%) was mixed. As the HTL, tris(4-carbazoyl-9-ylphenyl)amine) (TCTA, Lumtec, 99%) was used. The ITO sputter target (purity 99.95%) for the top electrode was purchased from Angstrom Engineering. As the antireflective coating, MgF_2 (Alfa Aesar, 99.995%) was used.

Device Fabrication: All thermally evaporated films were deposited under high vacuum conditions at $\approx 5 \times 10^{-7}$ mbar. For semitransparent A cells and substrate-configuration B^I, B^{II}, and B^{III} cells, prepatterned ITO (110 nm) glass substrates (Naranjo Substrates) were cleaned in the following sequence: sonication in acetone (15 min.), scrubbing and sonication in sodium dodecyl sulphate solution (Acros, 99%) in water (10 min.), rinsing in deionized water, and sonication in 2-propanol (15 min.). Prior to device preparation, the glass substrates were blow dried with nitrogen and further cleaned by UV-ozone (30 min.). For substrate-configuration C^{III} cells, Ni-plated high gloss steel (R1, HILAN, Tata Steel, R1), Ni-plated battery steel (HILUMIN, Tata Steel, R2), Cr-plated packaging steel (TCCT, Tata Steel, R3), and Zn-coated construction steel (MagiZinc Tata Steel, R4) substrates were cleaned in 2-propanol and blow dried with nitrogen. For all the steel substrates, a wire bar-coated polyamide-imide (PAI, Torlon Al-10, Solvay) was used as planarization layer. The planarization layer was cured in air at 265°C for 15 min. and cut to $3 \times 3 \text{ cm}^2$ samples for further use. Prior to the bottom electrode deposition, the samples were sonicated in isopropanol for 15 min and blow dried with N_2 . The solar cell fabrication on the PAI-coated R1–R4 steel substrates (stack C^{III}) was identical to the fabrication of stack B^{III}. For the Au-based substrate-configuration devices (stack B^I, B^{II}) a 120 nm patterned Au bottom electrode was deposited (1 \AA s^{-1}) onto the ITO glass substrate via thermal evaporation. For the Ti-based substrate-configuration devices (stack B^{III}, C^{III}), a 200 nm patterned Ti bottom electrode was deposited (2 \AA s^{-1}) onto the ITO glass substrate via electron-beam deposition. For all opaque substrate-configuration solar cells, a 10 nm patterned ITO interlayer was deposited ($\approx 0.3 \text{ \AA s}^{-1}$) via radio frequency magnetron sputtering under Ar/O_2 flow.

The SnO₂ dispersion was spin coated onto the ITO interlayer coated metal bottom electrodes on different substrates, at 2800 rpm (with a 2000 rpm s⁻¹ acceleration) for 60 s and heat treated at 150 °C for 30 min in ambient atmosphere. The SnO₂ (85 nm) film was then treated with UV-ozone (10 min.) and immediately transferred into a nitrogen-filled glovebox. To passivate the SnO₂ ETL, the PCBM or PCBA solution was spin coated onto the SnO₂ coated substrate at 2000 rpm (with a 2000 rpm s⁻¹ acceleration) for 30 s to leave a ≈1 nm thin passivation layer. For PCBM, the samples were annealed at 100 °C (30 min.) and cooled to room temperature. For PCBA no annealing was required. The Cs_{0.05}(MA_{0.17}FA_{0.83})_{0.95}Pb(I_{0.83}Br_{0.17})₃ perovskite film (≈600 nm thick) was processed using a ramped spin-coating deposition. The perovskite precursor solution was deposited statically onto the passivated ETL at 1000 rpm (200 rpm s⁻¹) for 10 s, which was followed by a ramp to 6000 rpm (2000 rpm s⁻¹). 10 s prior to the end of the spin-coating program 200 μL chlorobenzene was deposited. Prior depositing the HTL, the sample was annealed in the glovebox at 100 °C for 60 min. and cooled to room temperature. Thermally evaporated TCTA HTLs were deposited (2 Å s⁻¹) onto the perovskite films. The ITO top electrode (180 nm) was deposited (≈0.3 Å s⁻¹) using radio frequency sputtering under Ar/O₂ flow. For the devices with Au bottom electrode, MgF₂ was deposited via thermal evaporation. The active area (0.09 or 0.16 cm²) was determined by the overlap of the ITO, Au or Ti bottom electrode and the transparent ITO top electrode.

Device Characterization: All samples were stored and measured in a nitrogen-filled glovebox without any further exposure to air or any preconditioning, unless stated otherwise. The current density–voltage (*J*–*V*) characteristics were measured by a Keithley 2400 source meter. During the *J*–*V* measurements, light from a tungsten-halogen lamp was filtered by a Schott GG385 UV filter and a Hoya LB120 daylight filter to mimic the AM1.5G spectrum (100 mW cm⁻²). For top (ITO top electrode side) illumination of solar cells, a black shadow mask with an aperture area of 0.0676 or 0.1296 cm² was employed to define the illuminated cell area. During the fast *J*–*V* sweep measurements, the source meter swept the voltage either from +1.5 to –0.5 V (reverse scan) or from –0.5 to +1.5 V (forward scan) at a scan rate of 0.25 V s⁻¹. Light soaking preconditioning of the solar cells were performed by exposing the cell area to continuous illumination of simulated AM1.5G (100 mW cm⁻²) light for a given time, followed by a fast sweep measurement. For the stabilized *J*–*V* measurement (slow sweep measurements), the *V*_{oc} of the solar cell was first tracked for 5 min. under constant illumination and then a reverse sweep from *V*_{oc} + 0.04 V to –0.04 V was performed with a step size of 0.04 V, the acquisition time of the current density at each voltage step was 5 s. External quantum efficiency (EQE) measurements were performed in a nitrogen atmosphere. The probe light was generated by a 50 W tungsten-halogen lamp (Philips Focusline), which was modulated with a mechanical chopper (Stanford Research, SR 540) before passing through a monochromator (Oriel, Cornerstone 130). The spectral response of the device was recorded as a voltage from a pre-amplifier (Stanford Research, SR 570) using a lock-in amplifier (Stanford Research, SR 830), and was calibrated by a reference silicon cell. To accurately determine the short-circuit current density (*J*_{sc, EQE}), a green LED (530 nm, Thorlabs M530L3, driven by a DC4104 driver) was utilized as a light bias during the EQE measurement to provide the solar cell with approximately one sun equivalent illumination intensity.

Film Characterization: 3D surface profile maps for the planarization layer coated steel substrate were measured using a Dektak surface profiler (Bruker). AFM surface topologies were measured with a Veeco Dimension 3100 AFM in tapping mode. The root-mean-square roughness (*R*_q) and maximum profile peak height (*R*_p) values were estimated from these measurements.

Optical Simulation: Optical simulations were performed using the transfer matrix method with Setfos 5.0 (Fluxim AG). The wavelength dependent refractive indices for TCTA, sputtered ITO, triple-cation perovskite active layer and the Ti bottom electrode (*n*) and extinction coefficients (*k*) are depicted in Figure S3 (Supporting Information). The wavelength dependent *n* and *k* for the other layers can be found in our previous work from our group.^[24]

Supporting Information

Supporting Information is available from the Wiley Online Library or from the author.

Acknowledgements

This research was carried out under project number F71.4.15562b in the framework of the Partnership Program of the Materials innovation institute M2i and the Foundation of Fundamental Research on Matter (FOM) which is part of the Netherlands Organization for Scientific Research. The research also received funding from NWO Spinoza grant awarded to R.A.J. Janssen. The authors further acknowledge funding from the Ministry of Education, Culture and Science (Gravity program 024.001.035).

Conflict of Interest

The authors declare no conflict of interest.

Data Availability Statement

The data that support the findings of this study are available from the corresponding author upon reasonable request.

Keywords

metal-halide perovskites, optical modeling, solar cells, steel substrates

Received: October 27, 2021

Revised: December 20, 2021

Published online: January 6, 2022

- [1] M. A. Green, E. D. Dunlop, J. Hohl-Ebinger, M. Yoshita, N. Kopidakis, X. Hao, *Prog. Photovoltaics Res. Appl.* **2020**, *29*, 3.
- [2] T. James, A. Goodrich, M. Woodhouse, R. Margolis, S. Ong, Building-Integrated Photovoltaics (BIPV) in the Residential Sector: An Analysis of Installed Rooftop System Prices, USA **2011**, <https://doi.org/10.2172/1029857>.
- [3] K. Wojciechowski, D. Forgács, T. Rivera, *Sol. RRL* **2019**, *3*, 1900144.
- [4] H. Wang, J. Li, H. A. Dewi, N. Mathews, S. Mhaisalkar, A. Bruno, *J. Phys. Chem. Lett.* **2021**, *12*, 1321.
- [5] A. Extnance, *Nature* **2019**, *570*, 429.
- [6] X. Li, P. Li, Z. Wu, D. Luo, H.-Y. Yu, Z.-H. Lu, *Mater. Rep. Energy* **2020**, *1*, 100001.
- [7] V. Zardetto, T. M. Brown, A. Reale, A. Di Carlo, *J. Polym. Sci., Part B: Polym. Phys.* **2011**, *49*, 638.
- [8] L. Hughes, N. Bristow, T. Korochkina, P. Sanchez, D. Gomez, J. Kettle, D. Gethin, *Appl. Energy* **2018**, *229*, 209.
- [9] L. Cojocar, K. Wienands, T. W. Kim, S. Uchida, A. J. Bett, S. Rafizadeh, J. C. Goldschmidt, S. W. Glunz, *ACS Appl. Mater. Interfaces* **2018**, *10*, 26293.
- [10] K. Hamada, K. Yonezawa, K. Yamamoto, T. Taima, S. Hayase, N. Ooyagi, Y. Yamamoto, K. Ohdaira, *Jpn. J. Appl. Phys.* **2019**, *58*, SBBF06.
- [11] T. Abzieher, J. A. Schwenzer, S. Moghadamzadeh, F. Sutterluti, I. M. Hossain, M. Pfau, E. Lotter, M. Hetterich, B. S. Richards, U. Lemmer, M. Powalla, U. W. Paetzold, *IEEE J. Photovoltaics* **2019**, *9*, 1249.
- [12] M. Jošt, E. Köhnen, A. B. Morales-Vilches, B. Lipovšek, K. Jäger, B. Macco, A. Al-Ashouri, J. Krč, L. Korte, B. Rech, R. Schlatmann,

- M. Topič, B. Stannowski, S. Albrecht, *Energy Environ. Sci.* **2018**, *11*, 3511.
- [13] W. Qarony, M. I. Hossain, A. Salleo, D. Knipp, Y. H. Tsang, *Mater. Today Energy* **2019**, *11*, 106.
- [14] D. A. Jacobs, M. Langenhorst, F. Sahli, B. S. Richards, T. P. White, C. Ballif, K. R. Catchpole, U. W. Paetzold, *J. Phys. Chem. Lett.* **2019**, *10*, 3159.
- [15] P. Tockhorn, J. Sutter, R. Colom, L. Kegelmann, A. Al-Ashouri, M. Roß, K. Jäger, T. Unold, S. Burger, S. Albrecht, C. Becker, *ACS Photonics* **2020**, *7*, 2589.
- [16] J. H. Heo, D. H. Shin, M. L. Lee, M. G. Kang, S. H. Im, *ACS Appl. Mater. Interfaces* **2018**, *10*, 37.
- [17] B. T. Feleki, C. H. L. Weijtens, M. M. Wienk, R. A. J. Janssen, *ACS Appl. Energy Mater.* **2021**, *4*, 3033.
- [18] M. Saliba, T. Matsui, J.-Y. Seo, K. Domanski, J.-P. Correa-Baena, M. K. Nazeeruddin, S. M. Zakeeruddin, W. Tress, A. Abate, A. Hagfeldt, M. Grätzel, *Energy Environ. Sci.* **2016**, *9*, 1989.
- [19] J. Wang, K. Datta, C. H. L. Weijtens, M. M. Wienk, R. A. J. Janssen, *Adv. Funct. Mater.* **2019**, *29*, 1905883.
- [20] W. L. Liu, W. J. Chen, T. K. Tsai, S. H. Hsieh, C. M. Liu, *Thin Solid Films* **2006**, *515*, 2387.
- [21] W. L. Liu, W. J. Chen, T. K. Tsai, S. H. Hsieh, C. M. Liu, *Appl. Surf. Sci.* **2007**, *253*, 5516.
- [22] L. Tous, S. N. Granata, P. Choulat, T. Bearda, A. Michel, A. Uruena, E. Cornagliotti, M. Aleman, R. Gehlhaar, R. Russell, F. Duerinckx, J. Szlufcik, *Sol. Energy Mater. Sol. Cells* **2015**, *142*, 66.
- [23] N. Marinova, W. Tress, R. Humphry-Baker, M. I. Dar, V. Bojinov, S. M. Zakeeruddin, M. K. Nazeeruddin, M. Grätzel, *ACS Nano* **2015**, *9*, 4200.
- [24] B. T. Feleki, S. Chandrashekar, R. K. M. Bouwer, M. M. Wienk, R. A. J. Janssen, *Sol. RRL* **2020**, *4*, 2000385.